Crustal and uppermost mantle structure of Cape Verde from ambient noise tomography

J. Carvalho[1,*], G. Silveira[1,2], S. Kiselev[3], S. Custódio[1], R. S. Ramalho[1,4,5,6], E. Stutzmann[7] and Martin Schimmel[8]

[1]Instituto Dom Luiz (IDL), Faculdade de Ciências, Universidade de Lisboa, Campo Grande, 1749-016, Lisboa, Portugal

[2]Instituto Superior de Engenharia de Lisboa, Rua Conselheiro Emídio Navarro, 1, 1959-007, Lisboa, Portugal

[3]Institute of Physics of the Earth, Bolshaya Gruzinskaya str., 10-1 Moscow 123242, Russia

[4]School of Earth and Environmental Sciences, Cardiff University, Park Place, Cardiff, CF10 3AT, United Kingdom

[5]Departamento de Geologia, Faculdade de Ciências, Universidade de Lisboa, 1749-016 Lisboa, Portugal

[6]Lamont-Doherty Earth Observatory, Columbia University, Comer Geochemistry Building, PO Box 1000, Palisades, NY10964-8000, USA

[7]Université de Paris Cité, Institut de Physique du Globe de Paris, CNRS, 1 rue Jussieu, 75005 Paris, France

[8]Geosciences Barcelona, CSIC, 08028 Barcelona, Spain

Abbreviated Title: Cape Verde ambient-noise tomography

[*]Corresponding author email: jfcarvalho@fc.ul.pt

SUMMARY

We present a seismic ambient noise tomography of the Cape Verde archipelago, located in the Atlantic Ocean, approximately 600 km west of Senegal. We used 38 seismic broadband stations that continuously recorded for 10 months, in order to construct the first 3-D model of Sv-wave velocities for the crust and uppermost mantle beneath the Cape Verde region. We started by computing phase

cross-correlations for vertical component recordings using all possible inter-island station pairs. Next, a time-frequency phase-weighted stack was applied to obtain robust Rayleigh wave group velocity dispersion curves in the period band between 10 s and 24 s. Group-velocity maps at different periods are obtained by inverting the dispersion. We then inverted the group-velocity maps to obtain the 3D shear-wave velocity structure of the crust and uppermost mantle beneath Cape Verde. The final 3D model extends from 8 km down to 23 km and has a lateral resolution of about 50 km. The crust in the southwestern sector, encompassing Fogo, presents lower S-wave velocities that may be caused by the presence of melt pockets and/or hydrothermal fluids circulation. The uppermost mantle beneath the northwestern sector is characterized by higher S-wave velocities in agreement with previous results obtained from Ps and Sp receiver functions. Those high-velocity anomalies can reflect non-altered crust or remnants of magma chambers or solidified basaltic intrusions, which fed the volcanism in these islands. Our maps revealed the presence of crustal underplating across the entire archipelago, yet stronger beneath the groups Santo Antão – São Vicente – São Nicolau and Fogo – Santiago – Maio.

Key words: Seismic noise; Seismic tomography; Surface waves and free oscillations; Oceanic hotspots and intraplate volcanism; Crustal structure

1. INTRODUCTION

The relatively simple structure of the oceanic crust and sub-oceanic uppermost mantle, although dependent on age and drifting speed, becomes highly complex in the vicinity of within-plate volcanic regions (e.g. Leahy et al., 2010; Fontaine et al., 2015; Gorbatikov et al., 2013). The Cape Verde Archipelago, which has been formed over a hotspot, is no exception and is assumed to be more complex than its surroundings, attracting much interest. Moreover, Cape Verde is considered an example

of a stationary volcanic archipelago with respect to its melting source (McNutt, 1988), and so presumably its deep structure may reflect the effects of cumulative intrusive and magmatic processes, over an inferred 26 Ma lifetime of the hotspot.

Accurate three-dimensional (3D) models of the seismic structure beneath hotspots are of extreme importance to understand the mantle to surface mass transfer, as well as the lithospheric tectonic evolution, and further contributing to a better location of local earthquakes and seismic and volcanic hazard assessment. Several seismic studies have contributed to illuminating Cape Verde's deeper seismic structure (e.g. Helffrich et al. 2010; Vinnik et al. 2012; Carvalho et al. 2019b; Liu and Zhao, 2021). However, given the geometry of the seismic networks in the archipelago and the irregular distribution of the seismic events (Faria and Fonseca, 2014; Vales et al., 2014), crustal and uppermost mantle studies have been limited to 1D profiles beneath some of the islands (Lodge and Helffrich, 2006) or 2D seismic profiles across the entire Cape Verde Archipelago (e.g. Ali, 2003; Pim et al., 2008, Wilson et al., 2010; 2013). Our motivation is to investigate the structure of the crust and uppermost mantle beneath Cape Verde, generating a 3D shear-wave velocity model of the region.

Local earthquake tomography and controlled-source seismology are the methods most used to investigate the seismic structures of the crust and uppermost mantle. Nevertheless, the inadequate source-receiver geometry across Cape Verde does not allow local earthquake tomography and active-source seismology is extremely expensive.

For long, ambient seismic noise was considered a nuisance to be discarded from seismograms, obscuring seismic information in earthquake signals. However, nowadays, ambient noise is one of the fastest-growing fields in the Earth sciences and is widely applied for different purposes [e.g. hydrocarbon exploration (Bussat and Kugler, 2009); geological engineering (Picozzi et al. 2009); fluid injection monitoring (Stork et al. 2018), volcanism (Wang et al. 2017) or fault mapping (Brandmayr et al. 2016)]. Ambient seismic wavefield recordings are predominantly dominated by surface waves and can be widely recorded at periods which are suitable to image the Earth's crust and upper mantle.

These surface waves can be obtained by seismic interferometry and then analyzed by ambient noise tomography (ANT).

In the last decades, ANT has been successfully applied worldwide, at different scales: Regional scales, such as in the western United States (e.g. Moschetti et al. 2007; Shapiro et al. 2005), Madeira Island (Matos et al. 2015), West of Java, Indonesia (Pranata et al. 2019) or Costa Rica (Nuñez et al. 2019); continental scales such as Europe (Yang et al. 2007; Lu et al. 2018), North America (Bensen et al. 2008) and Australia (Saygin and Kennett, 2012) and even at global scales (e.g. Haned et al. 2016; Nishida et al. 2009).

In this study, we analyze continuous seismic data from a total of 38 broadband stations, temporarily deployed across the Cape Verde Islands (Weber et al. 2007) (Fig. 1b). Station pairs located on the same island were discarded due to the small inter-station distances. In total, we extracted empirical Green's functions (EGFs) from 6-hr long cross-correlations of the vertical component at 634 station pairs. We applied a Phase Cross-Correlation (PCC) processing technique, followed by a time-frequency Phase Weighted Stack (tf-PWS) developed by Schimmel et al. (2011). Inter-station group-velocity measurements obtained by S-transform (Schimmel et al., 2017) were then inverted to infer lateral perturbations of the group velocities through the Fast Marching Surface Tomography (FMST) method (Rawlinson and Sambridge, 2005). From these we obtained a 3D shear-wave velocity model, constraining the solid Earth structure from 8 km down to 23 km depth.

2. GEODYNAMIC SETTING

The volcanic Cape Verde Archipelago is composed of ten islands located in the eastern Atlantic Ocean [14º–18º N and 22º–26º W], 600 - 850 km off Senegal coast, West Africa (Fig. 1a). The islands are arranged in a west-facing horseshoe shape, with two diverging chains. The nonexistence of a linear track with a time-distance correlation between islands has been interpreted as a result of the closeness between the rotation pole for the Nubian plate and the archipelago (Burke and Wilson, 1972; Pollitz, 1991), which is thus considered nearly stationary over the melting source that fed the islands'

volcanism (McNutt, 1988; Lodge and Helffrich, 2006; Holm et al., 2008; Ramalho et al., 2010a). The islands rest on top of one of the largest bathymetric anomalies in the Earth's oceans – the Cape Verde Rise – which is considered a hotspot swell (e.g. Sleep, 1990; Pim et al., 2008; Wilson et al., 2010) thermally rejuvenated down to an age of 59 Ma (Sleep, 1990) or even to 30 Ma (Carvalho et al., 2019b).

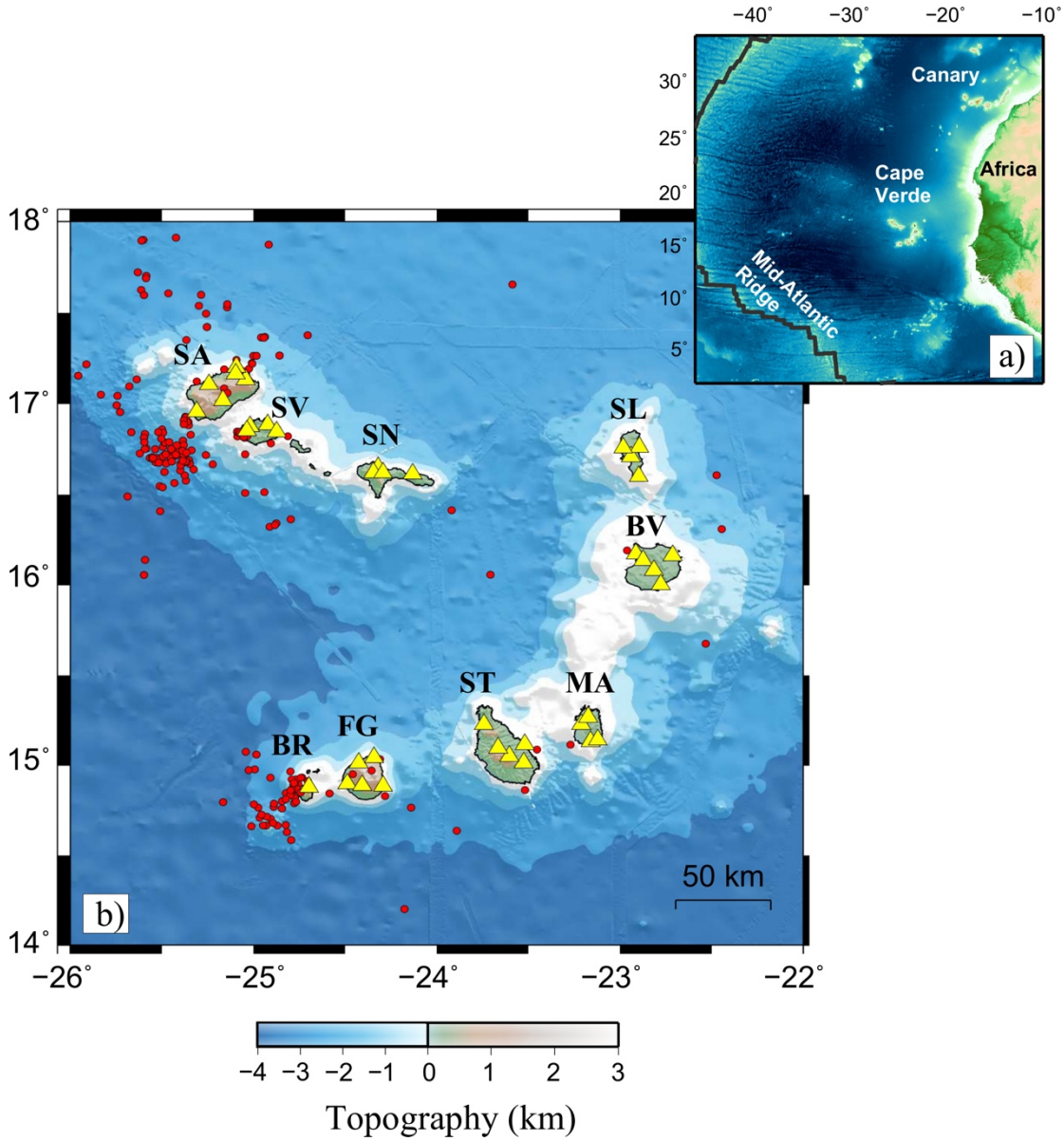

Figure 1: a) Topographic map of the Central Atlantic region. b) Geographic distribution of the islands, bathymetry of the archipelago (GEBCO Compilation Group, 2020) and abbreviated names of the islands: SA – Santo Antão; SV – São Vicente; SN – São Nicolau; SL – Sal; BV – Boavista; MA – Maio; ST – Santiago; FG – Fogo and BR – Brava. Triangles in yellow represent the 9A seismic

123 network (Weber et al., 2007), encompassing 38 stations, whereas the red circles represent the
124 seismicity between 2007 and 2008 detected by Vales et al. (2014), for depths ranging between 0 and
125 30 km.
126
127 Magnetic anomalies and bathymetric data suggest that the islands are placed on an ~80 km thick, old
128 oceanic lithosphere (120 to 140 Ma; Müller et al., 2008). Pim et al. (2008) proposed a regional oceanic
129 crust of ~7-13 km thickness beneath the Cape Verde swell. These values were later corroborated by
130 Wilson et al. (2010; 2013), based on seismic and gravimetric constraints. However, under the
131 individual islands, the crust appears to be thicker (10 – 22 km), as suggested by the analysis of Ps
132 receiver functions by Lodge and Helffrich (2006). Later, Vinnik et al. (2012), using a joint inversion
133 of Ps and Sp receiver functions for three different groups of islands, suggested an even thicker crust
134 (10 – 30 km), which they interpreted as due to the presence of a magmatic underplate layer. Recently,
135 Liu and Zhao (2021) presented a 1D V_S model, indicating a Moho depth across all archipelago at
136 approximately 15 ± 10 km.
137 Exposed volcanism in Cape Verde Archipelago dates to the Oligocene (25.6 ± 1.1 Ma) and extends
138 well into the Holocene (Torres et al., 2010). Historical eruptions (i.e. < 500 yrs) are unknown, except
139 on Fogo, where the last eruption occurred in 2014/15 (Mata et al. 2017 and references therein). A
140 faint age progression can be observed along the eastern-to-southern chain, which agrees
141 simultaneously with the age of the oldest exposed volcanic sequences, by the age progression of the
142 shield phase, both with ages decreasing towards the southwest, and with the progressively younger
143 volcanic morphology and relief of the islands towards the west (e.g Ramalho 2011; Samrock et al.,
144 2019).
145 Seismicity in the archipelago is sparse, detected essentially in the islands of Fogo, Brava, and Santo
146 Antão, as well as offshore, typically related to volcano-tectonic activity and to active seamounts or
147 submarine cone fields (e.g. Grevemeyer et al., 2010; Faria and Fonseca, 2014; Leva et al., 2019).
148 Vales et al. (2014), using the same seismic network as in this study, analyzed the seismicity of the

149 region, and confirmed that most earthquakes are concentrated in the westernmost areas of the
150 archipelago (Fig. 1b).

151 **3. DATA AND EMPIRICAL GREEN FUNCTIONS**

152 We processed continuous seismic waveform data from 38 temporary stations of the 9A network
153 (Weber et al., 2007) [Fig. 1b)]. These stations were equipped with Earth Data PR6-24 data loggers
154 and Guralp CMG-3ESP seismometers and recorded during 10 months from December 2007 until
155 September 2008, with a sampling rate of 100 Hz. Inter-station distances vary from ~22.5 km to ~295
156 km, not counting stations on the same island.
157 For each station, continuous vertical-component seismic data were cut into 6-hr length segments. The
158 corresponding 6-hr time series were down sampled from the original 100 Hz to 2 Hz, demeaned and
159 detrended. The instrument response was removed in order to obtain ground velocities and the
160 seismograms were then band-pass filtered in the 0.03 - 0.5 Hz frequency band.
161 The subsurface properties between two seismic receivers are expressed by Green's Functions. To
162 determine the EGFs we applied the phase correlation (PCC), followed by the time-frequency phase
163 weighted stack (tf-PWS), as proposed by Schimmel et al. (2011). PCC is amplitude unbiased and
164 therefore do not require time-domain normalization or spectral whitening in order to remove un-
165 wanted signals or to reduce the effect of high energy signals such as earthquakes (Schimmel, 1999;
166 Schimmel et al., 2011).
167 PCC were calculated for 634 inter-station pairs, for time lags between -300 and 300, which includes
168 the surface wave train at the longest inter-station distances. Instead of the traditional linear stacking
169 procedure, we then applied the tf-PWS stacking of Schimmel et al. (2011). Previous studies jointly
170 applied the PCC and the tf-PWS methods and demonstrated that they result in improved signals and
171 more robust group-velocity measurements (e.g. Haned et al. 2016; Corela et al. 2017; Poveda et al.
172 2018; Hable et al. 2019; Nuñez et al. 2019; Acevedo et al. 2019). For more details on these methods
173 the reader is referred to Schimmel and Gallart (2007) and to Schimmel et al. (2011).

Inter-station paths and corresponding EGFs sorted by their inter-station distance are shown in Figs. 2a and 2b. EGFs were constructed by stacking both the causal and acausal segments for each station pair, after time-reversing the acausal part. Some asymmetries can be observed on EFGs, which is a consequence of the heterogeneous distribution of the seismic noise sources (Carvalho et al. 2019a). Since we are working with the ZZ components (i.e., cross-correlations between vertical-component seismograms), we expect EGFs to consist mainly of Rayleigh waves. Indeed, Fig. 2 shows prominent wave arrivals corresponding to the expected propagation velocities, between 1.8 – 3.6 km/s. A second slower arrival is also visible, with velocities ranging between 1.0 – 1.3 km/s. This second wave train is mainly detected in the EGFs corresponding to station pairs separated by deep ocean. Other authors have previously detected such a second wave package with significantly lower velocity in oceanic environments on empirical Green's functions measured between OBS (e.g. Hable et al., 2019; Le et al., 2018).

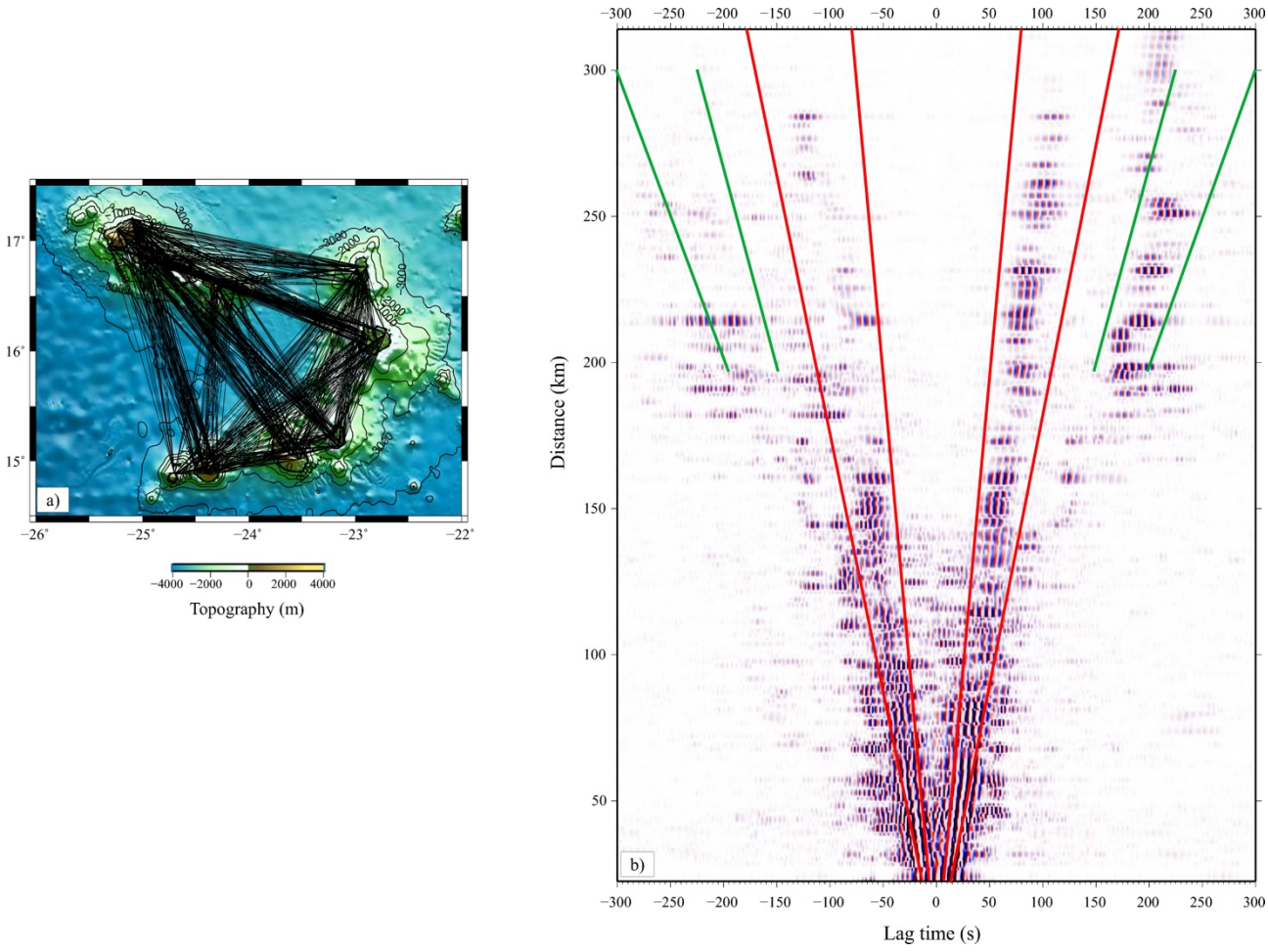

Figure 2: a) Inter-station paths corresponding to the 634 station pairs for which EGFs were computed. b) EGFs sorted by inter-station distance. The red lines delimit the Rayleigh-wave arrivals, with velocities between 1.8 - 3.6 km/s. A slower arrival is also seen bounded by green lines, with velocities between 1.0 - 1.3 km/s.

4. AMBIENT SEISMIC NOISE GROUP-VELOCITY MEASUREMENTS

In order to measure group velocity dispersion curves, we applied the strategy developed by Schimmel et al. (2017), for a robust and semi-automated estimation of group velocities from energy diagrams, based on the S-transform and using a resampling approach. The S-transform uses frequency-dependent scaling windows in comparison to the wavelet transform, overcoming some of its disadvantages (Stockwell et al., 1996). It has proven to be a powerful tool to transform the empirical Green's functions in the time-frequency domain.

For extracting group velocity values that can be associated with Rayleigh waves, we defined a velocity range of 1.5 - 4.5 km/s for Rayleigh wave measurements, based on the record section of Fig. 2. We also selected a frequency range of 0.03 - 0.5 Hz (T ~2 - 30 s). Fig. 3 shows an example of the group-velocity measurements calculated for the inter-station path CVBV1 - CVSA4. The same procedure was applied to all possible station pairs, with the exception, of those located on the same island, as mentioned before. In most of the energy diagrams we observed that amplitudes are very high for a broad range of group velocities at high frequencies (above 0.1 Hz), thus the automated procedure has some difficulty in selecting single dispersion measurement in this range (Fig.3).

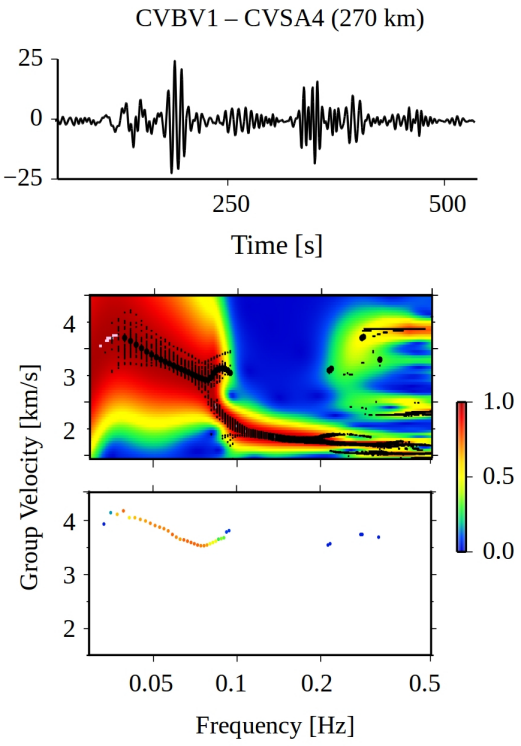

217

218 **Figure 3:** EGFs obtained in the frequency band 0.03 - 0.5 Hz for the inter-station path CVBV1-
219 CVSA4 (270 km long; top panel), the corresponding energy diagram (middle panel) where the black
220 dots mark all the detected maxima, and the selected dispersion curve (bottom panel).

221

222 In Figure 3 we can observe that the code automatically selects a few measurements at higher frequen-
223 cies (which seem to be an overtone) but because the next measurements to be considered exhibit
224 much lower velocities, they are not accounted. The code is prepared to avoid these oscillations. Thus,
225 the next signals to be considered are the ones below 0.1 Hz, where there is only one clear measure-
226 ment. Despite the detection of black dots (maxima) in the entire frequency band, the presence of
227 multiple signals, especially at higher frequencies (above 0.1 Hz), prevents the code from correctly
228 selecting a dispersion curve for these. In several other measurements, even when an energy-dominant
229 signal fits the established parameters, the code selected what seems to be overtones (Fig S1.1). To
230 overcome this problem, we tested the approach of Haned et al. (2016), later also followed by Hable
231 et al. (2019), and filtered each trace into three narrower frequency bands (0.03 – 0.1 Hz 0.1 – 0.2 Hz

and 0.2 – 0.5 Hz). However, this procedure did not improve significantly our group-velocity measurements (Fig. S1.2) as it did not allow to follow a continuous group velocity as a function of frequency. All the dispersion curves were finally quality checked manually, so that we kept only dispersion curves free of ambiguity. Fig. 4 shows all the selected dispersion curves. In general, the measured dispersion curves are consistent with each other, clustering into a single group. Most dispersion measurements exhibit rapidly changing velocities at ~0.1 Hz and multiple dispersion branches, probably overtones, making impossible to follow the fundamental-mode group velocity as a function of frequency. This same behavior was found in other studies where paths cross both water and land (Corela et al., 2017) or a larger water portion compared to the land portion (Hable et al., 2019, Schlaphorst et al., 2021). This feature seems to be characteristic of oceanic environments and both Hable et al. (2019) and Schlaphorst et al. (2021) discarded all dispersion measurements for frequencies higher than 0.1 Hz.

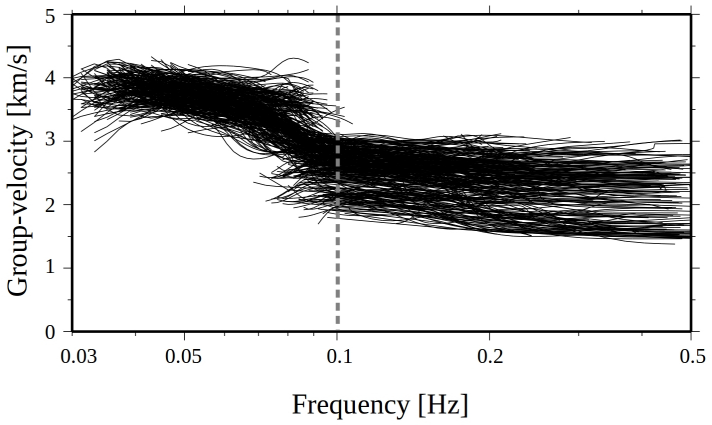

Figure 4: Measured dispersion curves for all possible inter-station paths (after removal of outliers). The dashed grey line separates the curves discarded (above 0.1 Hz) from the ones used in the tomography (below 0.1 Hz).

Considering the detected multiple signals in most energy diagrams above 0.1 Hz, and the automatically selected dispersion curves (Fig. 3), we modeled Rayleigh-wave fundamental mode synthetics in a laterally varying medium to verify if the fundamental mode was properly isolated from the overtones (Herrmann et al., 2013). This analysis (see supporting information for detailed explanation)

shows not only that the fundamental mode is not clearly separated from higher modes but also that the water layer has a clear influence on high-frequency (> 0.1 Hz) Rayleigh wave dispersion measurements.

In the Cape Verde area, the ocean has a depth of 3 to 4 km between some islands. According to our synthetic group velocity dispersion curves (see Fig. S2.2 of supporting information), we then expect that for frequencies higher than 0.1 Hz the fundamental mode is not clearly separated from the higher modes. Thus, Rayleigh-wave group-velocity dispersion curves for frequencies above 0.1 Hz will not be considered in our tomographic computations. In future work, we intend to investigate the feasibility of using Love waves in order to improve the resolution of our models and eventually image the structure below the current 23 km depth. In fact, it is important to take into consideration the Love waves in ambient noise tomography of oceanic environments, since these waves are not affected by the water layer (Pinzon et al., 2019).

5. TOMOGRAPHY

To obtain a 3D model of S-wave velocity we followed a commonly applied surface wave tomography two-step approach. In the first step, we computed maps with the lateral variation of group-velocity, as a function of period, using the Fast Marching Surface Tomography (FMST) method of Rawlinson and Sambridge (2005); in the second step, we inverted the group-velocity maps by using a trans-dimensional inversion technique to obtain the local S-wave velocity at each grid-point as a function of depth (Haned et al. 2016; Silveira et al., 2022).

5.1 Group-velocity maps

FMST is a non-linear tomographic inversion suitable to determine group velocity maps for different periods that relies on two steps: 1) prediction of travel-times (forward problem) and 2) adjustment of the model parameters that best match the data, using regularization constrains (inverse problem).

The 2D model of group velocities for each period is parameterized with 150 velocity nodes, over a grid spaced 0.4 deg in latitude x 0.3 deg in longitude, which constitute the inversion grid. A constant initial velocity was taken from the average group velocity dispersion curve to initialize the inversion. Several synthetic checkerboard tests were performed, with different grids spacings, in order to decide the final grid dimension and thus to estimate the maximum available resolution with the current network design (Fig S3 of the supporting information). Fig. 5 shows the input synthetic checkerboard group velocity map, with the final grid-cell size, as well as the recovered anomalies for $T \sim 11$, 17 and 20 s, for the chosen grid spacing and regularization parameters. Despite the challenging distribution of the network, which results from the distribution of the islands in a horse-shoe shape and from the lack of OBSs to fill the oceanic gaps, the resolution tests indicate that a well-resolved velocity model for the considered period range (10 - 24 s) can be obtained. The number of inter-station paths is similar for all selected periods, which results in similar resolution at all periods. Measurements for inter-station distances shorter than two wavelengths were discarded as they tend to represent poorly the sampled structure.

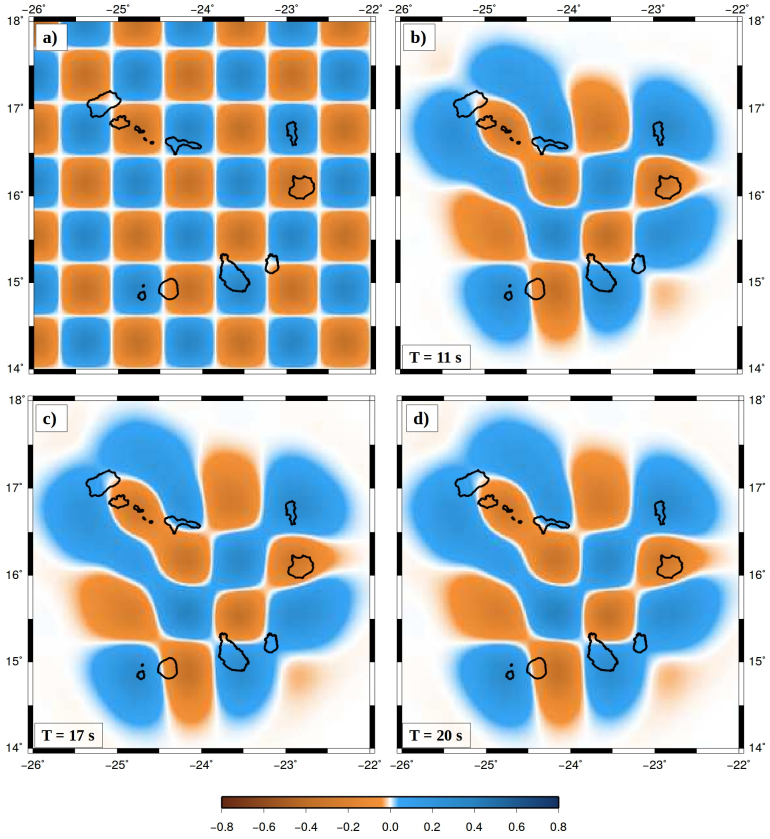

Figure 5: Synthetic input checkerboard [panel a)] and the recovered output anomalies for T = 11, 17 and 20 s [panel b), c) and d), respectively].

The regularization parameters applied to stabilize the inversion, smoothing (η) and damping (ε), were chosen after repeated iterations, for different values of damping and smoothing, as in Rawlinson et al. (2006). We varied the damping factor from 0.5 to 50 and determined that ε = 5 represents a good compromise between data misfit (RMS) and model variance. The same procedure was applied to determine the smoothing parameter. We now varied the smoothing from 1 to 750, after fixing the damping parameter at 5. A good compromise between data misfit (RMS) and model roughness was found for η = 50. In general, the impact of these parameters on the inversion result was rather low. The L-shaped trade-off curves in Fig. S3 represent the variation of the RMS data-misfit as a function of model roughness, model variation and number of iterations in those tests. For the chosen parameters, ε = 5 and η = 50, the inversion converges quickly after three iterations (Fig. S4).

Fig. 6 presents our final group velocity maps for periods of 10, 14 and 18 s, as well as the corresponding ray coverage. Slower and faster than average velocities are presented with warmer and cooler colors, respectively. Complete results for all periods are available in the supporting information (Fig. S5).

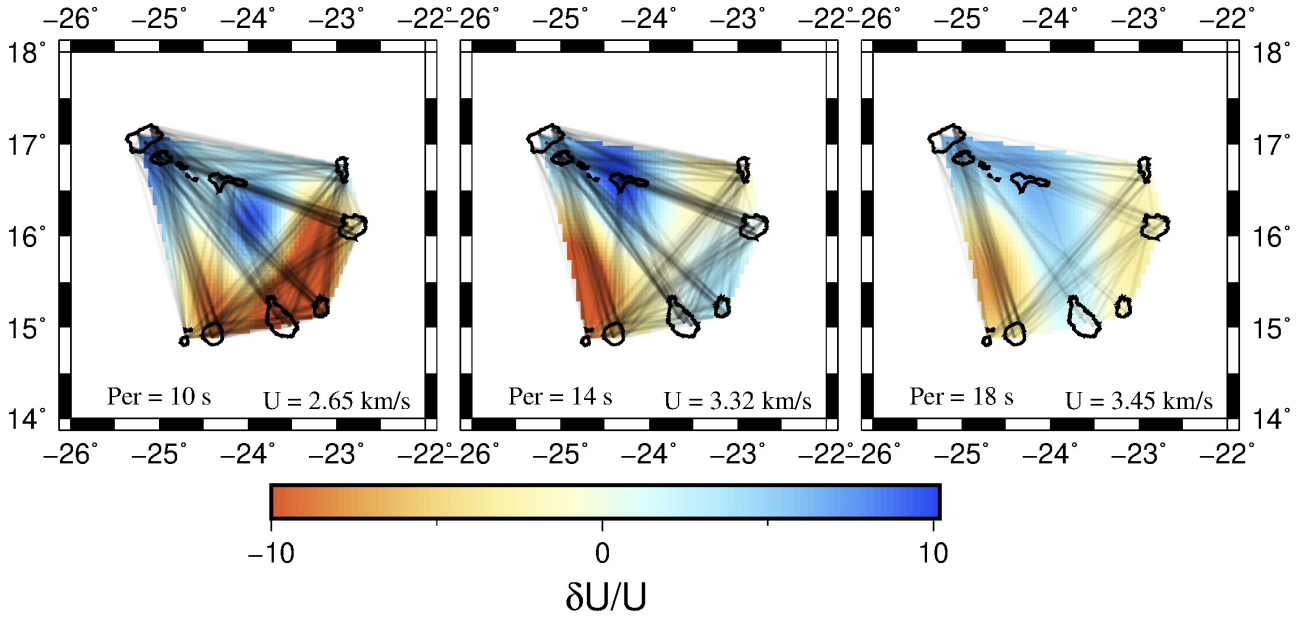

Figure 6: Rayleigh-wave group velocity maps for selected periods of 10 s, 14 s, and 18 s. Black lines represent the inter-station paths used for each period.

The group velocity maps display higher velocities in the northwestern group of islands, for the entire period band. In opposition, the islands of Fogo and Brava exhibit lower velocities at all periods.

5.2 S-wave velocity model

Next, the group-velocity maps were inverted to obtain the tomographic S-wave velocity model as described in Haned et al. (2016) and Silveira et al. (2022). The inversion performed here is identical to the one applied in Silveira et al. (2022). For this study a water layer was included on the a priori model and the group velocity measurements were only considered below 0.1 Hz.

The inversion is computed for each point of a grid of 0.05º x 0.05º in latitude and longitude. At each grid point, synthetic group velocities are computed for different periods assuming a given S-wave velocity model, as a function of depth.

The inverse problem is non-unique unless a smoothing condition is imposed on the trial S-wave velocity model. The Moho discontinuity must also be considered. To integrate both conditions, the S-wave velocity model is represented as the sum of the *a priori* model with discontinuities plus a continuous and smoothed curve expressed as a series of B-spline basis functions with weight coefficients,

which are the model parameters. The absence of shorter periods is handled by the inversion code using a higher level of regularization (i.e, the inverse of the number of splines).

In Haned et al. (2016) the crustal model was taken from crust1.0 (Laske et al., 2013) to obtain their tomographic model. Here, as we work at a small scale and in an oceanic environment, we determine a uniform a priori S-wave velocity in the crust. Our *a priori* model consists of a water layer and an uniform layer for the crustal part followed by the PREM (Dziewonski and Anderson, 1981) for the mantle.

In our *a priori* model the Moho depth is given by Lodge and Helffrich (2006) for the islands and Pim et al. (2008) for the oceanic basin. Due to the wavelength of surface waves, which does not allow the resolution of small-scale changes in Moho depth, we smoothed the depth lateral variations of the Moho, with a correlation length L_{cor} = 50 km.

After smoothing, Moho depths vary in the narrow range from 11.9 to 13 km (Fig. 7a), showing that the oceanic Moho depth dominates due to the small size of the islands. Following the same approach, in order to compute the water layer, the bathymetric map of the region was also smoothed (Fig. 7b). We can see that after smoothing the *a priori* model has a water layer even in the islands.

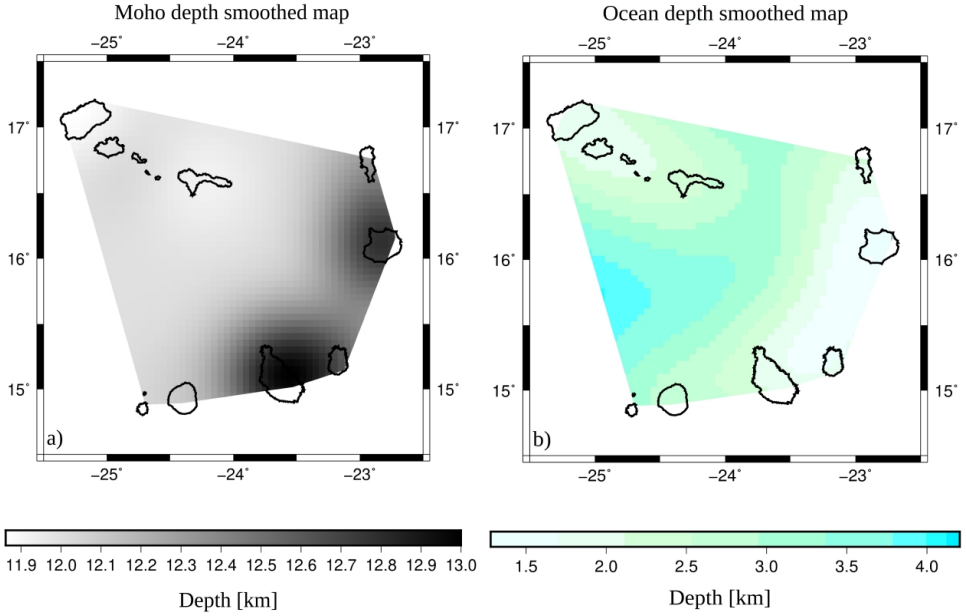

Figure 7: a) Map of smoothed Moho depth showing that Moho depths vary in a narrow range between 11.9 to 13 km. b) Smoothed bathymetric map displaying the existence of a water layer in the *a priori* model, even in the islands.

Sensitivity kernels indicate that the Rayleigh wave group velocities are mostly sensitive to structure down to about 30 km (Fig. S6). Therefore, we consider that our S-wave model can be interpreted until a depth of approximately 30 km, which contains information on the crust and uppermost mantle structure.

Fig. 8 presents the tomography slices at different depths. Each plot shows the distribution of S-wave velocities at selected depths in percentage with respect to the average velocity value at each depth. The average S-wave velocity value is plotted on the top-right corner of each slice, for reference.

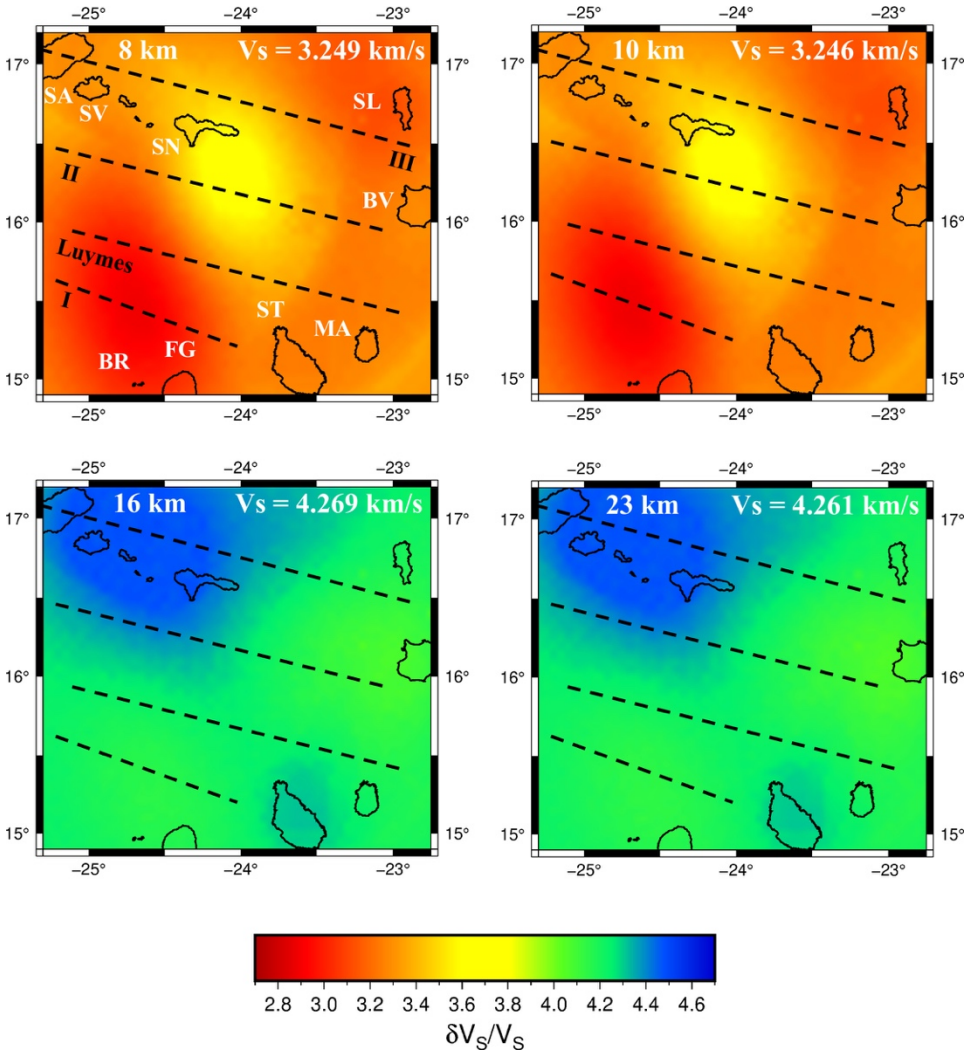

Figure 8: S-wave velocity models at different depths resulting from the inversion of group velocity maps. Velocities are plotted as absolute values. The depth and laterally averaged S-wave velocities are indicated at the top of each map. Velocity variations range from 2.7 to 4.7 km/s. Dashed lines represent the fracture zones proposed by Williams et al. (1990). We included their names on the top left map, as well as the abbreviated names of the islands: SA – Santo Antão; SV – São Vicente; SN – São Nicolau; SL – Sal; BV – Boavista; MA – Maio; ST – Santiago; FG – Fogo and BR – Brava.

At most depths the velocity exhibits smooth variations, as would be expected from a surface wave tomography. In the top 10 km, our model displays lower velocities beneath the islands and between Fogo and Santo Antão. The lowest values occur in the area beneath Brava and Fogo. From 10 km down to 23 km, the velocities increase in all the studied area, however the area beneath the northwestern islands exhibits a clear higher velocity, which seems to have some expression also beneath Santiago. The areas beneath the remaining islands show velocities close to the average. These anomalies are consistent down to the limit of our model (~ 23 km depth).

Fig. 9 presents several vertical profiles that extend from 8 km down to 18 km (with vertical exaggeration). These cross sections show low shear-wave velocities from approximately 8 to 13 km depth consistently in all the archipelago. However, as already observed in Fig. 8, the velocities are lower surrounding the island of Fogo and higher close to São Nicolau. At approximately 12 – 14 km depth, we detect the presence of a lenticular shaped higher velocity. Deeper, and as already observed in Fig. 8, most of the velocities become close to the average shear-wave velocity, with exception of the group of Santo Antão – São Vicente – São Nicolau, which exhibits higher velocities.

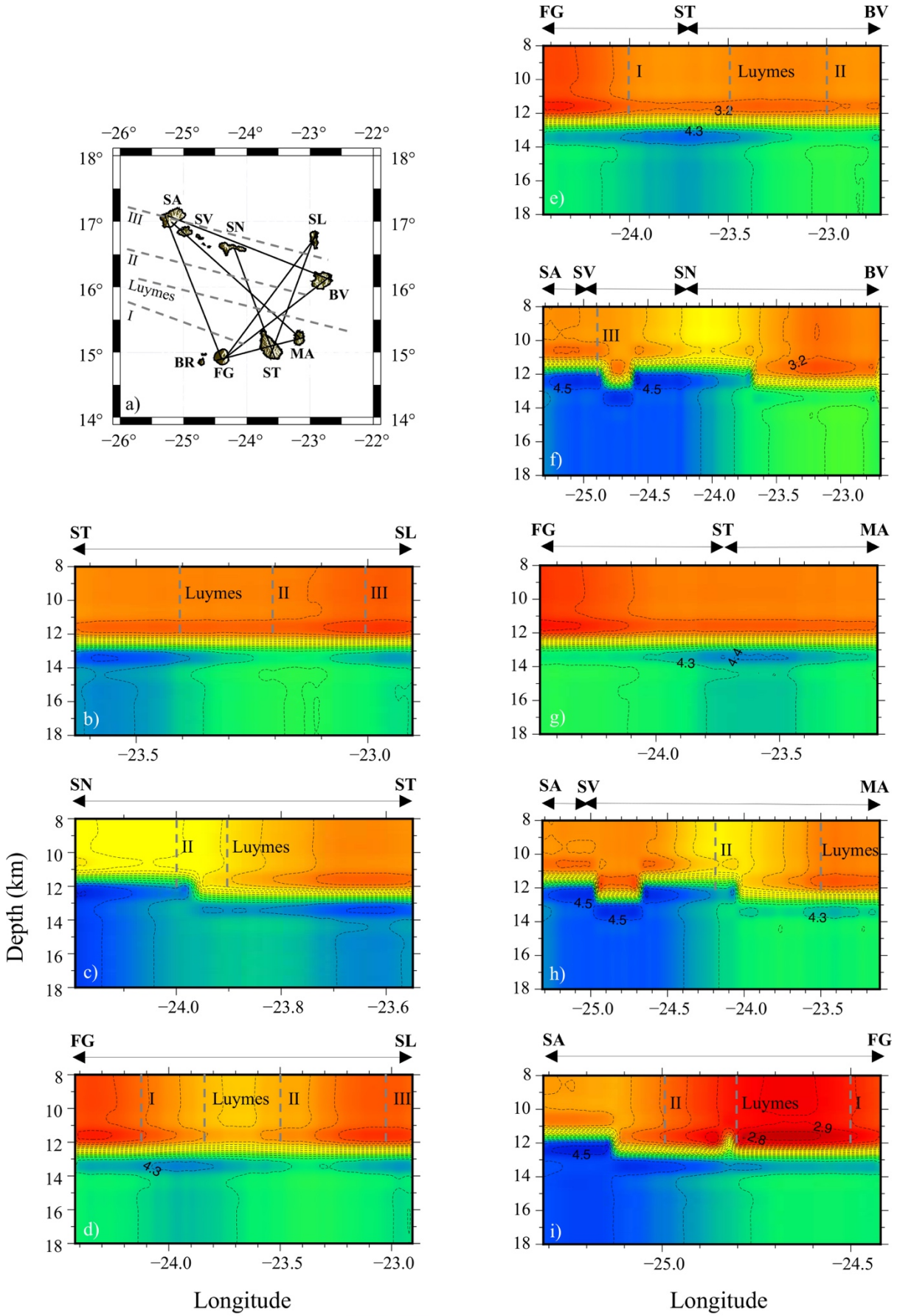
a)
SA
SV
SN
SL
BV
MA
BR
FG
ST
III
II
Luymes
I
b)
c)
d)
e)
f)
g)
h)
i)
Depth (km)
Longitude
Longitude
Vs (km/s)
2.8
3.2
3.6
4.0
4.4

Figure 9: a) Simplified topographic map of Cape Verde showing the selected profiles, the abbreviated names of the islands and the fracture zones (dashed lines) published in Williams et al. (1990). b) – i) Vertical profiles through the 3D shear wave velocities, represented in absolute velocities. Vertical dashed lines show the fracture zones identified in a).

6. DISCUSSION

Our 3D shear-wave velocity model offers new insights on the structure beneath Cape Verde at crustal and uppermost mantle depths, contributing with important information on the upper structure of this region (8 to ~23 km). At shallow depths (< 12 km) the islands are characterized, in general, by lower velocities than those of the oceanic area between São Nicolau and Santiago. At those depths, the lowest velocities are found to the north-northwest of Fogo, between fracture zones I, Luymes and II, as can be seen in Fig 9i). Fogo and Brava are the youngest and (presently) most active volcanoes in the archipelago. For the top few km (~ 12 km), corresponding to the crust, the low-velocity anomaly in this region may be the result of a much higher predominance of melt pockets, in good agreement with the active volcanism observed in this part of the archipelago. Fogo and Brava also exhibit the thinnest crust (e.g. Lodge and Helffrich, 2006; Vinnik et al., 2012) and are the sites of ongoing intrusive processes at crustal and uppermost mantle levels, as demonstrated by the recorded seismicity and recent volcanism (see Faria and Fonseca, 2014; Leva et al., 2019; Vales et al., 2014). These characteristics suggest a hotter, melt-rich crust and uppermost mantle beneath and in the vicinities of these islands, in contrast with the rest of the archipelago, where crustal seismic velocities are higher. The extension of this anomaly further to the north is somewhat enigmatic, but it may suggest that melt pockets – or recent intrusions – at shallower levels are more widespread than previously thought. It is worth mentioning that the northwest terminus of the archipelago was also the site of recent vigorous volcanism and exhibits recorded seismicity attesting to volcanic unrest and consequently active volcanism (Faria and Fonseca, 2014; Vales et al., 2014; Eisele et al., 2015); intriguingly, however, the lower shear-wave velocities do not fully extend to the northwest terminus of the

442 archipelago. As such, the observed shear-wave velocity reduction could also eventually be explained
443 by more intense hydrothermal alteration of the oceanic crust in this area, leading to a reduction in
444 shear-wave velocities.
445 The analysis of compressional to shear (P to S) converted seismic phases by Lodge and Helffrich
446 (2006) pointed to a Moho discontinuity shallower beneath the Santo Antão and São Nicolau, and
447 deeper beneath the remaining islands. Although neither the Moho depth nor the Vs velocity discon-
448 tinuity at Moho depth are resolvable by surface waves, the distribution of the S-wave velocities in
449 profiles f, h and i of Fig. 9 seem to support that the Moho depth is indeed shallower at Santo Antão
450 and São Nicolau than below the remaining islands.
451 Deeper, between 13 and 15 km, most of the islands exhibit the presence of a thin shell characterized
452 by higher velocities than the underlying mantle. We suggest these high-velocity lower-crustal bodies
453 are the result of underplating processes, considered by some authors an integral part of intraplate
454 volcanism in oceanic lithosphere (e.g Caress et al., 1995). Crustal thickening (by cumulative intru-
455 sions) and underplating have also been suggested as an important feature in Cape Verde, inclusively
456 leading to the modification of the architecture of the archipelago's flexural moat (Ali et al., 2003) and
457 being responsible for significant island uplift trends (Ramalho et al., 2010a,b; Ramalho, 2011).
458 Below 14 – 15 km, in the uppermost mantle, we observe that the S-wave velocities are particularly
459 higher beneath the northwest group and slightly higher close to the island of Santiago as also observed
460 by Vinnik et al. (2012) (Fig. S6). In their study, the 1D shear wave velocity model obtained from
461 simultaneous inversion of combined Ps and Sp receiver functions measured in São Vicente and São
462 Nicolau, display higher velocities between 10 and 20 km depth, than at SALA (Sal station) and
463 SACV+MLOS (Santiago and Fogo combined) These higher velocities below the northwest of the
464 archipelago could reflect solidified remnants of magma reservoirs, which fed the volcanism in these
465 islands, and that which are now significantly colder than in the terminus of the eastern-to-southern
466 chain.
467

7. CONCLUSIONS

We imaged the 3D S-wave structure of the upper 23 km below the Cape Verde archipelago based on Rayleigh-wave group velocities measured from ambient noise phase cross-correlations, in a period band between 10 s to 24 s. Our results show shear-wave absolute velocities, varying between 2.7 to 4.6 km/s at each depth.

At crustal levels, the lowest velocities were found beneath and around the islands of Fogo and Brava. We attributed these low velocities to active volcanism and to a predominance of melt pockets or less likely to a stronger hydrothermal alteration of the crust. Descending into the upper mantle, the velocity increases quite sharply, especially beneath the northwest islands where the velocity becomes clearly higher than in the rest of the archipelago. The higher shear-wave velocities in that area are interpreted as remnants of magma reservoirs, which fed the volcanism of the northwest islands. The remaining islands show velocities close to the average below ~13 km. Shear wave velocity profiles support previous findings of a shallower Moho beneath the islands of Santo Antão and São Nicolau than beneath the other islands. Beneath all islands, with exception of Boavista, lenticular shaped high-velocity layers stand out below the crust. We speculate that these layers could be the result of crustal underplating processes that took place during hotspot volcanism.

The results presented in this study are in good agreement with previous studies, which due to the data and/or methodology limitations could not resolve the Cape Verde upper structure (crust and uppermost mantle). Ambient noise tomography is a useful technique in imaging the crust and upper mantle features beneath oceanic islands, where other techniques (e.g. local earthquake tomography) are not suitable. However, we faced two major limitations: the uneven distribution of interstation paths due to the island's geometry, and the effect of a water layer which made it difficult to measure unambiguously fundamental mode dispersion velocities at frequencies above 0.1 Hz. To overcome these problems, a deployment of regularly spaced ocean-bottom seismometers would allow the improvement of the azimuthal coverage. On the other hand, cross-correlations of the horizontal components would also allow the observation of Love waves, which are not sensitive to the water.

ACKNOWLEDGEMENTS

This study was supported by Fundação para a Ciência e a Tecnologia (FCT) project SIGHT (Ref. PTDC/CTA-GEF/30264/2017) and it is also a contribution to FCT projects FIRE (Ref. PTDC/GEO-GEO/1123/2014) and RESTLESS (PTDC/CTA-GEF/6674/2020). This work was also developed in the framework of FCT UIDB/50029/2020 - Instituto Dom Luiz. Joana Carvalho was supported by FCT under the PhD grant PD/BD/114480/2016 and under the project PTDC/CTA-GEF/30264/2017. Ricardo S. Ramalho acknowledges his former IF/01641/2015 fellowship funded by FCT. Martin Schimmel thanks SANIMS (RTI2018-095594-B-I00). All figures were made using GMT – Generic Mapping Tools (Wessel et al., 2013). Data pre-processing was done using SAC – Seismic Analysis code (Goldstein and Snoke, 2005).

8. DATA AVAILABILITY STATEMENT

The data underlying this article are available in GEOFON data centre at https://geofon.gfz-potsdam.de/doi/network/9A/2007, and can be accessed under the network code 9A.

520 **REFERENCES**

521 Acevedo, J., Fernández-Viejo, G., Llana-Fúnez, S., López-Fernández, C., & Olona, J. (2019). Ambi-
522 ent noise tomography of the southern sector of the Cantabrian Mountains, NW Spain. *Geophysical*
523 *Journal International*, *219*(1), 479–495. 10.1093/gji/ggz308

524 Ali, M. Y., Watts, A. B., & Hill, I. (2003). A seismic reflection profile study of lithospheric flexure
525 in the vicinity of the Cape Verde Islands. *Journal of Geophysical Research: Solid Earth*, *108*(B5), 1–
526 24. 10.1029/2002JB002155

527 Bensen, G. D., Ritzwoller, M. H., & Shapiro, N. M. (2008). Broadband ambient noise surface wave
528 tomography across the United States. *Journal of Geophysical Research: Solid Earth*, *113*(5), 1–21.
529 10.1029/2007JB005248

530 Brandmayr, E., Kuponiyi, A. P., Arroucau, P., & Vlahovic, G. (2016). Group velocity tomography of
531 the upper crust in the eastern Tennessee seismic zone from ambient noise data. *Tectonophysics*, *688*,
532 148–156. 10.1016/j.tecto.2016.09.035

533 Burke, K., & Wilson, J. (1972). Is the African Plate stationary? *Nature*, 239(5372), 387–390.

534 Bussat, S. and Kugler, S., 2009. Recording noise estimating shear wave veloc- ities: feasibility of
535 off-shore ambient-noise surface-wave tomography on a reservoir scale, in 79th Annual International
536 Meeting, SEG, Expanded Abstracts, 1627–1631.

537 Caress, D. W., McNutt, M. K., Detrick, R. S., & Mutter, J. C. (1995). Seismic imaging of hotspot-
538 related crustal underplating beneath the Marquesas Islands. *Nature*, *373*(6515), 600-6003.

539 Carvalho, J., Bonadio, R., Silveira, G., Lebedev, S., Mata, J., Arroucau, P., … Celli, N. L. (2019).
540 Evidence for high temperature in the upper mantle beneath Cape Verde archipelago from Rayleigh-
541 wave phase-velocity measurements. *Tectonophysics*, *770* (October), 228225.
542 https://doi.org/10.1016/j.tecto.2019.228225

543 Carvalho, J. F., Silveira, G., Schimmel, M., & Stutzmann, E. (2019). Characterization of Microseis-
544 mic Noise in Cape Verde. *Bulletin of the Seismological Society of America*, *109*(3), 1099–1109.
545 10.1785/0120180291

546 Corela, C., Silveira, G., Matias, L., Schimmel, M., & Geissler, W. H. (2017). Ambient seismic noise
547 tomography of SW Iberia integrating seafloor- and land-based data. *Tectonophysics*, *700–701*, 131–
548 149. 10.1016/j.tecto.2017.02.012
549 Eisele, S., Freundt, A., Kutterolf, S., Ramalho, R.S., Kwasnitschka, T., Wang, K.L. & Hemming,
550 S.R., (2015). Stratigraphy of the Pleistocene, phonolitic Cão Grande Formation on Santo Antão, Cape
551 Verde. Journal of Volcanology and Geothermal Research, 301, pp.204-220.
552 Dziewonski, A. M. and Anderson, D. L. (1981). Preliminary reference Earth model. Physics of the
553 earth and planetary interiors, 25(4), 297-356.
554 Faria, B. and Fonseca, J. F. B. D. (2014). Investigating volcanic hazard in Cape Verde Islands through
555 geophysical monitoring: Network description and first results. Natural Hazards and Earth System
556 Sciences, 14(2), 485–499. 10.5194/nhessd-1-4997-2013
557 Fontaine, F. R., Barruol, G., Tkalčić, H., Wölbern, I., Rümpker, G., Bodin, T., & Haugmard, M.
558 (2015). Crustal and uppermost mantle structure variation beneath La Réunion hotspot track. *Geo-*
559 *physical Journal International*, *203*(1), 107-126. 10.1093/gji/ggv279
560 GEBCO Compilation Group (2020) GEBCO 2020 Grid (doi:10.5285/a29c5465-b138-234d-e053-
561 6c86abc040b9)
562 Goldstein, P., and A. Snoke (2005). SAC availability for the IRIS community, Incorporated Research
563 Institutions for Seismology Newsletter, 7 (UCRL-JRNL-211140).
564 Gorbatikov, A. V., Montesinos, F. G., Arnoso, J., Stepanova, M. Y., Benavent, M., & Tsukanov, A.
565 A. (2013). New features in the subsurface structure model of El Hierro Island (Canaries) from low-
566 frequency microseismic sounding: An insight into the 2011 seismo-volcanic crisis. *Surveys in Geo-*
567 *physics*, *34*(4), 463-489. 10.1007/s10712-013-9240-4
568 Grevemeyer, I., Helffrich, G., Faria, B., Booth-Rea, G., Schnabel, M. and Weinrebe, W. (2010). Seis-
569 mic activity at Cadamosto seamount near Fogo Island, Cape Verdes - formation of a new ocean is-
570 land? Geophysical Journal International, 180(2), 552-558.

Hable, S., Sigloch, K., Stutzmann, E., Kiselev, S., & Barruol, G. (2019). Tomography of crust and lithosphere in the western Indian Ocean from noise cross-correlations of land and ocean bottom seismometers. *Geophysical Journal International*, *219*(2), 924–944.

Haned, A., Stutzmann, E., Schimmel, M., Kiselev, S., Davaille, A., & Yelles-Chaouche, A. (2016). Global tomography using seismic hum. *Geophysical Journal International*, *204*(2), 1222–1236. 10.1093/gji/ggv516

Hariharan, A., Dalton, C. A., Ma, Z. and Ekström, G. (2020). Evidence of Overtone Interference in Fundamental - Mode Rayleigh Wave Phase and Amplitude Measurements. Journal of Geophysical Research: Solid Earth, 125(1), 1–17.

Helffrich, G., Faria, B., Fonseca, J. F. B. D., Lodge, A., & Kaneshima, S. (2010). Transition zone structure under a stationary hot spot: Cape Verde. *Earth and Planetary Science Letters*, *289*(1–2), 156–161. https://doi.org/10.1016/j.epsl.2009.11.001

Herrmann, R. B. (2013). Computer Programs in Seismology: An Evolving Tool for Instruction and Research. *Seismological Research Letters*, *84*(6), 1081–1088. 10.1785/0220110096

Holm, P.M., Grandvuinet, T., Friis, J., Wilson, J.R., Barker, A.K. and Plesner, S., 2008. An ^{40}Ar-^{39}Ar study of the Cape Verde hot spot: Temporal evolution in a semi-stationary plate environment. *Journal of Geophysical Research: Solid Earth*, 113(B8).

Laske, G., Masters, G., Ma, Z., & Pasyanos, M. (2013). Update on CRUST1. 0—A 1-degree global model of Earth's crust. In *Geophys. res. abstr* (Vol. 15, p. 2658).

Le, B.M., Yang, T., Chen, Y.J. & Yao, H., (2018). Correction of OBS clock errors using Scholte waves retrieved from cross-correlating hydrophone recordings, Geophys. J. Int., 212(2), 891–899.

Leahy, G. M., Collins, J. A., Wolfe, C. J., Laske, G., & Solomon, S. C. (2010). Underplating of the Hawaiian Swell: evidence from teleseismic receiver functions. *Geophysical Journal International*, *183*(1), 313-329.

595 Leva, C., Rümpker, G., Link, F., anf Wölbern, I. (2019). Mantle earthquakes beneath Fogo volcano,
596 Cape Verde: Evidence for subcrustal fracturing induced by magmatic injection. Journal of Volcanol-
597 ogy and Geothermal Research, 386, 106672.
598 Liu, X., & Zhao, D. (2021). Seismic evidence for a plume-modified oceanic lithosphere–astheno-
599 sphere system beneath Cape Verde. *Geophysical Journal International*, *225*(2), 872–886.
600 https://doi.org/10.1093/gji/ggab012
601 Lodge, A., & Helffrich, G. (2006). Depleted swell root beneath the Cape Verde Islands. *Geology*,
602 *34*(6), 449. 10.1130/G22030.1
603 Lu, Y., Stehly, L., Paul, A., & AlpArray Working Group. (2018). High-resolution surface wave to-
604 mography of the European crust and uppermost mantle from ambient seismic noise. *Geophysical*
605 *Journal International*, *214*(2), 1136-1150. 10.1093/gji/ggy188
606 Mata, J., Martins, S., Mattielli, N., Madeira, J., Faria, B., Ramalho, R., Silva, P., Moreira, M., Cal-
607 deira, R., Moreira, M., et al., 2017. The 2014-15 eruption and the short-term geochemical evolution
608 of the Fogo volcano (Cape Verde): evidence for small-scale mantle heterogeneity. Lithos 288–289,
609 91–107. 10.1016/j.lithos. 2017.07.001.
610 Matos, C., Silveira, G., Matias, L., Caldeira, R., Ribeiro, M. L., Dias, N. A., … Bento dos Santos, T.
611 (2015). Upper crustal structure of Madeira Island revealed from ambient noise tomography. *Journal*
612 *of Volcanology and Geothermal Research*, *298*(June), 136–145. 10.1016/j.jvolgeores.2015.03.017
613 McNutt, M. (1988). Thermal and mechanical properties of the Cape Verde Rise. *Journal of Geophys-*
614 *ical Research (Solid Earth)*, 93(B4), 2784–2794.
615 Moschetti, M. P., Ritzwoller, M. H., & Shapiro, N. M. (2007). Surface wave tomography of the west-
616 ern United States from ambient seismic noise: Rayleigh wave group velocity maps. *Geochemistry,*
617 *Geophysics, Geosystems*, *8*(8), 1–10. 10.1029/2007GC001655
618 Müller, R. D., Sdrolias, M., Gaina, C., & Roest, W. R. (2008). Age, spreading rates, and spreading
619 asymmetry of the world's ocean crust. *Geochemistry, Geophysics, Geosystems*, *9*(4).

620 Nettles, M. and Dziewonski, A. M. (2011). Effect of Higher-Mode Interference on Measurements
621 and Models of Fundamental-Mode Surface-Wave Dispersion. Bulletin of the Seismological Society
622 of America, 101(5), 2270–2280.
623 Nishida, K., Montagner, J. P., & Kawakatsu, H. (2009). Global surface wave tomography using seis-
624 mic hum. *Science*, *326*(5949), 112. https://doi.org/10.1126/science.1176389
625 Nuñez, E., Schimmel, M., Stich, D., & Iglesias, A. (2019). Crustal Velocity Anomalies in Costa Rica
626 from Ambient Noise Tomography. *Pure and Applied Geophysics*. 10.1007/s00024-019-02315z
627 Picozzi, M., Parolai, S., Bindi, D., & Strollo, A. (2009). Characterization of shallow geology by high-
628 frequency seismic noise tomography. *Geophysical Journal International*, *176*(1), 164-174.
629 Pim, J., Peirce, C., Watts, A. B., Grevemeyer, I., & Krabbenhoeft, A. (2008). Crustal structure and
630 origin of the Cape Verde Rise. *Earth and Planetary Science Letters*, *272*(1–2), 422–428.
631 10.1016/j.epsl.2008.05.012
632 Pinzon, J. I., Silveira, G. M., Custodio, S., Matias, L. M., Krueger, F., Dahm, T., ... & Carvalho, J.
633 (2019, December). How are ambient noise dispersion curves recorded in OBSs affected by the water?.
634 In *AGU Fall Meeting Abstracts* (Vol. 2019, pp. S23C-0649).
635 Pollitz, F. (1991). Two-stage model of African absolute motion during the last 30 million years. Tec-
636 tonophysics,194(1–2), 91–106.
637 Poveda, E., Julià, J., Schimmel, M., & Perez-Garcia, N. (2018). Upper and middle crustal velocity
638 structure of the Colombian Andes from ambient noise Tomography: Investigating subduction-related
639 magmatism in the overriding plate. *Journal of Geophysical Research: Solid Earth*, *123*(2), 1459-
640 1485. 10.1002/2017JB014688
641 Pranata, B., Yudistira, T., Widiyantoro, S., Brahmantyo, B., Cummins, P. R., Saygin, E., … Cipta,
642 A. (2019). Shear wave velocity structure beneath Bandung basin, West Java, Indonesia from ambient
643 noise tomography. *Geophysical Journal International*, 1045–1054. 10.1093/gji/ggz493

644 Ramalho, R., Helffrich, G., Cosca, M., Vance, D., Hoffmann, D., Schmidt, D.N. (2010a) Episodic
645 hotspot swell growth inferred from variable uplift from the Cape Verde hot spot Islands. *Nature Ge-*
646 *oscience*, Vol3, 774-777.
647 Ramalho, R.; Helffrich, G.; Cosca, M.; Vance, D.; Hoffmann, D.; Schmidt, D.N. (2010b) Vertical
648 movements of ocean island volcanoes: insights from a stationary plate. Marine Geology, vol. 275, pp
649 84-95.
650 Ramalho, R. A. (2011). Building the Cape Verde islands. In *Springer Theses*. 10.1007/978-3-642-
651 19103-9
652 Rawlinson, Nicholas, & Sambridge, M. (2005). *The fast marching method: an effective tool for tomo-*
653 *graphic imaging and tracking multiple phases in complex layered media*. *36*(4), 341–350.
654 Rawlinson, N., Reading, A. M., & Kennett, B. L. (2006). Lithospheric structure of Tasmania from a
655 novel form of teleseismic tomography. *Journal of Geophysical Research: Solid Earth*, *111*(B2).
656 Romanowicz, B. (2002). Inversion of surface waves: a review. International Geophysics Series,
657 81(A), 149-174.
658 Saygin, E. and Kennett, B. L. N. (2012). Crustal structure of Australia from ambient seismic noise
659 tomography. Journal of Geophysical Research: Solid Earth, 117(1), 1–15.
660 Samrock, L.K., Wartho, J.A. and Hansteen, T.H., 2019. ^{40}Ar-^{39}Ar geochronology of the active pho-
661 nolitic Cadamosto Seamount, Cape Verde. *Lithos*, 344, pp.464-481.
662 Schlaphorst, D., Harmon, N., Kendall, J. M., Rychert, C. A., Collier, J., Rietbrock, A., ... & VoiLA
663 Team. (2021). Variation in upper plate crustal and lithospheric mantle structure in the greater and
664 Lesser Antilles from ambient noise tomography. *Geochemistry, Geophysics, Geosystems*, *22*(7),
665 e2021GC009800.
666 Schimmel, Martin. (1999). Phase cross-correlations: Design, comparisons, and applications. *Bulletin*
667 *of the Seismological Society of America*, *89*(5), 1366–1378.

668 Schimmel, M., & Gallart, J. (2007). Frequency-dependent phase coherence for noise suppression in
669 seismic array data. *Journal of Geophysical Research: Solid Earth*, *112*(B4), 1–14.
670 10.1029/2006JB004680
671 Schimmel, M., Stutzmann, E., & Gallart, J. (2011). Using instantaneous phase coherence for signal
672 extraction from ambient noise data at a local to a global scale. *Geophysical Journal International*,
673 *184*(1), 494–506. 10.1111/j.1365-246X.2010.04861.x
674 Schimmel, Martin, Stutzmann, E., & Ventosa, S. (2017). Measuring Group Velocity in Seismic Noise
675 Correlation Studies Based on Phase Coherence and Resampling Strategies. *IEEE Transactions on*
676 *Geoscience and Remote Sensing*, *55*(4), 1928–1935. 10.1109/TGRS.2016.2631445
677 Silveira, G., Dias, N. A., Kiselev, S., Stutzmann, E., Custódio, S., Schimmel, M. (2022). Imaging the
678 crust and uppermost mantle structure of Portugal (West Iberia) with seismic ambient noise. Geophys-
679 ical Journal International, 230(2), 1106-1120. 10.1093/gji/ggac106
680 Shapiro, N. M., Campillo, M., Stehly, L., & Ritzwoller, M. H. (2005). High-Resolution Surface-Wave
681 Tomography from Ambient Seismic Noise. *Science*, *307*(5715), 1615–1618. 10.1086/275028
682 Sleep, N. H. (1990). Hotspots and mantle plumes: Some phenomenology. Journal of Geophysical
683 Research: Solid Earth, 95(B5), 6715-6736.
684 Stockwell, R. G., Mansinha, L., & Lowe, R. P. (1996). Localization of the complex spectrum: the S
685 transform. *IEEE transactions on signal processing*, *44*(4), 998-1001.
686 Stork, A.L., Allman, C., Curtis, A., Kendall, J.M. & White, D.J., 2018. Assessing the potential to use
687 repeated ambient noise seismic tomography to detect CO2 leaks: application to the Aquistore storage
688 site, Int. J. Greenhouse Gas Control, 71, 20–35.
689 Stutzmann, E. and Montagner, J. P. (1993). An inverse technique for retrieving higher mode phase
690 velocity and mantle structure. Geophysical Journal International, 113(3), 669-683.
691 Torres, P., Silva, L., Munhá, J., Caldeira, R., Mata, J., & Tassinari, C. C. (2010). Petrology and geo-
692 chemistry of lavas from Sal Island: implications for the variability of the Cape Verde magmatism.
693 *Comunicações Geológicas*.

694 Vales, D., Dias, N. A., Rio, I., Matias, L., Silveira, G., Madeira, J., … Haberland, C. (2014). Intraplate
695 seismicity across the Cape Verde swell: A contribution from a temporary seismic network. *Tectono-*
696 *physics*, *636*, 325–337. 10.1016/j.tecto.2014.09.014
697 Vinnik, L., Silveira, G., Kiselev, S., Farra, V., Weber, M., & Stutzmann, E. (2012). Cape Verde
698 hotspot from the upper crust to the top of the lower mantle. *Earth and Planetary Science Letters*,
699 *319–320*, 259–268. 10.1016/j.epsl.2011.12.017
700 Wang, Y., Lin, F.C., Schmandt, B. & Farrell, J., 2017. Ambient noise tomography across Mount St.
701 Helens using a dense seismic array, J. geophys. Res., 122, 4492–4508.
702 Weber, M. Silveira, G. and Schulze, A. (2007): The COBO/CV-PLUME temporary seismic network.
703 GFZ Data Services. Other/Seismic Network. doi:10.14470/4N7552467332.
704 Wessel, P., W. H. Smith, R. Scharroo, J. Luis, and F. Wobbe (2013). Generic Mapping Tools: Im-
705 proved version released, Eos Trans. AGU 94, no. 45, 409–410.
706 Williams, C. A., Hill, I. A., Young, R., & White, R. S. (1990). Fracture zones across the Cape Verde
707 rise, NE Atlantic. *Journal of the Geological Society*, *147*(5), 851-857.
708 Wilson, D. J., Peirce, C., Watts, A. B., Grevemeyer, I. and Krabbenhoeft, A. (2010). Uplift at
709 lithospheric swells - I: Seismic and gravity constraints on the crust and uppermost mantle structure
710 of the Cape Verde mid-plate swell. Geophysical Journal International, 182(2), 531–550.
711 10.1111/j.1365-246X.2010.04641.x
712 Wilson, D. J., Peirce, C., Watts, A. B., and Grevemeyer, I. (2013). Uplift at lithospheric swells—II:
713 is the Cape Verde mid-plate swell supported by a lithosphere of varying mechanical strength?. *Geo-*
714 *physical Journal International*, *193*(2), 798-819. 10.1093/gji/ggt034
715 Yang, Y., Ritzwoller, M. H., Levshin, A. L. and Shapiro, N. M. (2007). Ambient noise Rayleigh
716 wave tomography across Europe. Geophysical Journal International, 168(1), 259–274.
717
718